Phase fields of nickel silicides obtained by mechanical alloying in the nanocrystalline state

M. K. Datta, S. K. Pabi, and B. S. Murty[a)]
Department of Metallurgical and Materials Engineering, Indian Institute of Technology, Kharagpur 721 302, India

(Received 29 September 1999; accepted for publication 8 March 2000)

Solid state reactions induced by mechanical alloying (MA) of elemental blends of Ni and Si have been studied over the entire composition range of the Ni–Si system. A monotonous increase of the lattice parameter of the Ni rich solid solution, Ni(Si), is observed with refinement of crystallite size. Nanocrystalline phase/phase mixtures of Ni(Si), Ni(Si)+$Ni_{31}Si_{12}$, $Ni_{31}Si_{12}$+Ni_2Si, Ni_2Si+NiSi and NiSi+Si, have been obtained during MA, over the composition ranges of 0–10, 10–28, 28–33, 33–50, and >50 at. % Si, respectively. The results clearly suggest that only congruent melting phases, $Ni_{31}Si_{12}$, Ni_2Si, and NiSi form, while the formation of noncongruent melting phases, Ni_3Si, Ni_3Si_2, and $NiSi_2$, is bypassed in the nanocrystalline state. The phase formation during MA has been discussed based on thermodynamic arguments. The predicted phase fields obtained from effective free energy calculations are quite consistent with those obtained during MA. © *2000 American Institute of Physics.* [S0021-8979(00)00412-6]

I. INTRODUCTION

Transition metal silicides have been identified as highly promising candidates for diverse fields of application, which stems from their unique range of properties, such as high melting point, low density, excellent electrical conductivity, and high resistance to oxidation and corrosion. However, due to their narrow composition range and high melting points, processing of these intermetallics by conventional methods is extremely difficult. In this context, mechanical alloying (MA), which involves low temperature solid state reactions, provides an attractive alternative route for the synthesis of these intermetallics.[1–4] In addition, the feasibility of producing these intermetallics in the nanocrystalline state has widened the scope of MA.

Solid state reactions between a thin film of Ni and Si substrate during annealing have been studied by many researchers.[5–7] The motivation behind such a study is the technological importance of these materials in improving the performance of integrated circuits. Recently, solid state reactions between Ni and Si induced by MA of elemental Ni and Si powders has been investigated by several researchers.[8–11] Omuro and Miura[8] have reported the formation of Ni– silicides during MA of elemental blends of $Ni_{100-x}Si_x$ for $x=25$, 28, 33, and 50 in the early stages of milling, which transformed into an amorphous state with further milling except for the compositions $x=25$ and 50. Radlanski and Calka[9] and Omuro and Miura,[10] have shown that the final milled powder is a mixture of Ni_2Si and $Ni_{31}Si_{12}$ for the elemental blend of 30 at. % Si. On the other hand, formation of complete fcc solid solution of Si in Ni has been reported by Jang *et al.*[11] during MA of nominal composition 24 at. % Si. Recent investigation by Zhou and Bakker,[12] Jang and Tsau,[13] and Cho and Koch[14] on the ball milled samples of ordered $L1_2$–Ni_3Si, have revealed an antisite disordered structure in the early stages of milling and a phase transformation from the disordered Ni_3Si to fcc solid solution of Si in Ni on prolong milling.

In spite of the above reports, the evolution of various silicides in the nanocrystalline state during MA in the Ni–Si system has not been clearly understood so far. In the present study, MA has been carried out over a wide composition range in this system to synthesize nanocrystalline Ni–silicides and thermodynamic concepts have been utilized to understand the underlying solid state reactions.

II. EXPERIMENTAL DETAILS

Figure 1 shows the equilibrium Ni–Si phase diagram[15] with the compositions chosen for the study. Mixtures of el-

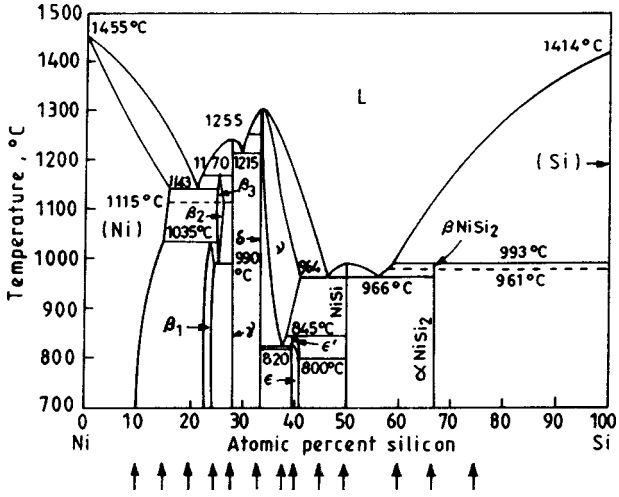

FIG. 1. Ni–Si phase diagram with the compositions chosen for MA.

a)Author to whom correspondence should be addressed; present address: National Research Institute for Metals, Tsukuba 305-0047, Japan; electronic mail: murty@nrim.go.jp

TABLE I. Nickel silicides with their experimentally estimated heat of formation ΔH_f and melting points T_m.

Phase	at. % Si	$-\Delta H_f$ (kJ/mol)	T_m (°C)
β-Ni_3Si(NC)[a]	22.8–24.5	36	1143
γ-$Ni_{31}Si_{12}$(C)[b]	27.9	42	1242
δ-Ni_2Si(C)[b]	33.3	48	1306
ϵ-Ni_3Si_2(NC)[a]	40	46	—
η-NiSi(C)[b]	50	45	992
$NiSi_2$(NC)[a]	66.7	31	993

[a](NC) noncongruent melting phase.
[b](C) congruent melting phase.

emental powders of Ni and Si of 99.5% purity and $\leqslant 45$ μm size, corresponding to nominal compositions $Ni_{100-x}Si_x$ ($x = 10$, 15, 20, 25, 28, 33, 37, 40, 45, 50, 60, 67 and 75) were subjected to milling in a planetary ball mill (FRITSCH Pulverisette-5) in toluene. The milling was carried out at 300 rpm up to 30 h in a WC container using 10 mm diameter WC balls with a ball to powder weight ratio of 10:1. The milling was interrupted at regular intervals to collect samples for analysis by x-ray diffraction (XRD). The XRD studies were performed on a PHILIPS 1710 x-ray diffractometer using Co K_α ($\lambda = 0.178\,89$ nm) radiation. The effective crystallite size was calculated by Voigt function using the single line method[16] after eliminating the strain and instrumental broadening contribution. The effective crystallite size of Ni, Si, and different intermetallic phases and the volume fraction of these phases have been calculated from their most intense peaks in the XRD patterns.

The composition of the mechanically alloyed powders after 30 h of MA was analyzed using energy dispersive x-ray (EDX) microanalyzer, attached to a transmission electron microscope (TEM). PHILIPS CM30 operating at 200 kV, was employed for the TEM observations to evaluate the crystallite size and chemical composition of the mechanically alloyed samples.

TABLE II. Phases obtained after 30 h of MA with their compositions and the corresponding equilibrium phases.

Si content of the initial blend (at. %)	Si content after 30 h of milling (at. %)	Phases present after 30 h of MA	Equilibrium phases at RT[a] at milled compositions
10	9.1	Ni(Si)	Ni(Si)
15	13.2	Ni(Si)+$Ni_{31}Si_{12}$	Ni(Si)+ord.Ni_3Si
20	18.2	Ni(Si)+$Ni_{31}Si_{12}$	Ni(Si)+ord.Ni_3Si
25	22.9	$Ni_{31}Si_{12}$+Ni(Si)	ord.Ni_3Si
28	25.7	$Ni_{31}Si_{12}$+Ni(Si)	ord.Ni_3Si+$Ni_{31}Si_{12}$
33	30.9	Ni_2Si+$Ni_{31}Si_{12}$	Ni_2Si+$Ni_{31}Si_{12}$
37	35.1	Ni_2Si+NiSi	Ni_2Si+Ni_3Si_2
40	37.0	Ni_2Si+NiSi	Ni_2Si+Ni_3Si_2
45	42.7	Ni_2Si+NiSi	Ni_3Si_2+NiSi
50	48.1	Ni_2Si+NiSi	Ni_3Si_2+NiSi
60	58.3	NiSi+Si	NiSi+$NiSi_2$
67	65.2	NiSi+Si	NiSi+$NiSi_2$
75	73.2	NiSi+Si	$NiSi_2$+Si

[a]RT: room temperature.

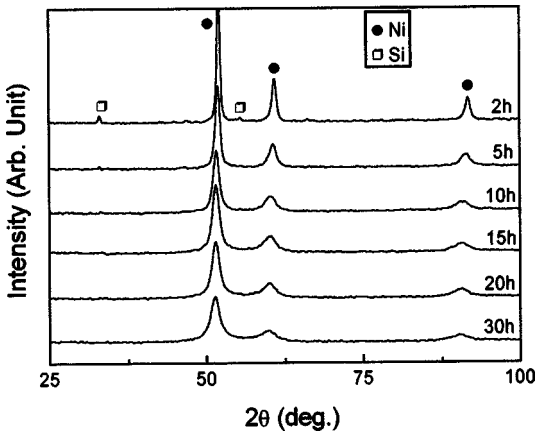

FIG. 2. XRD patterns of 10 at. %Si as a function of milling time.

III. RESULTS

Table I lists the silicides of the Ni–Si system along with their experimentally estimated heats of formation[17] and melting temperatures.[15] The end product compositions (analyzed by EDX microanalyzer) and phases formed after 30 h of MA are shown in Table II as a function of the initial blend composition along with the corresponding equilibrium phase(s) expected at the end product compositions. It is evident from Table II that the composition of the alloy after 30 h of MA has shifted from that of the original elemental blend toward a lower Si content suggesting some loss of Si during milling. If one compares the heats of formation of Si and Ni oxides (-304 and -120 kJ/mol for SiO_2 and NiO, respectively), it is quite reasonable to assume that oxygen will preferentially react with Si during MA. Thus, the phases formed after MA corresponds to those of lower Si content (by about 2%) than the original blend.

A. Composition range: $10 \leqslant x \leqslant 28$

The XRD patterns taken after different duration of milling for $x = 10$ are shown in Fig. 2. The diffraction peaks of Si have disappeared after 20 h of milling, suggesting the formation of complete fcc solid solution of Si in Ni (Ni(Si)). The increased incorporation of Si into Ni is known to decrease the lattice parameter of the later.[18] However, it is interesting to note that the position of Ni peaks continuously shifted to

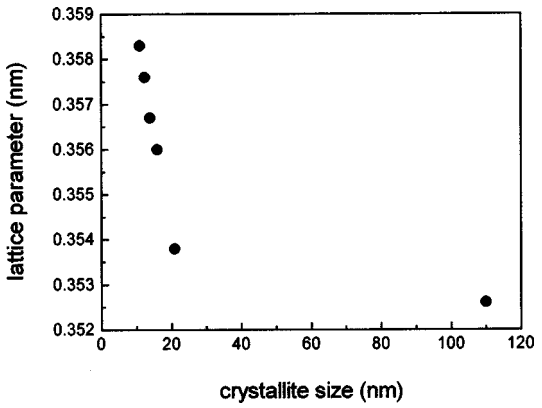

FIG. 3. Variation of lattice parameter with crystallite size of 10 at. %Si.

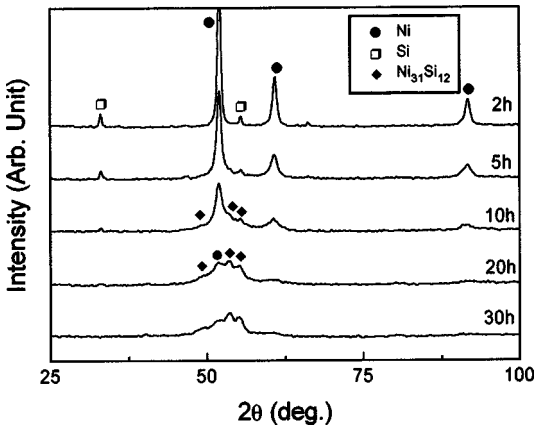

FIG. 4. XRD patterns of 25 at. %Si at various milling times.

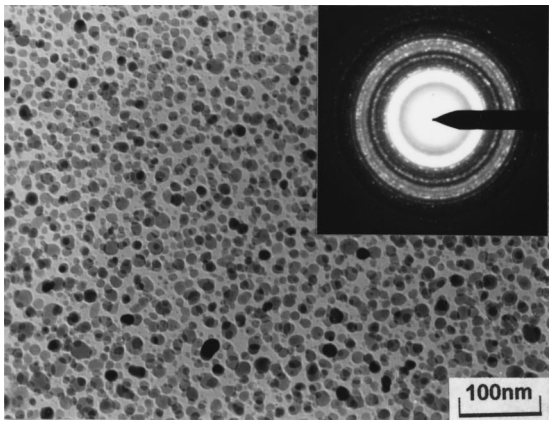

FIG. 6. Transmission electron micrograph and selected area diffraction pattern (inset) of 25 at. %Si milled for 30 h showing nanocrystalline $Ni_{31}Si_{12}$.

lower angles with milling time, indicating a continuous increase in its lattice parameter with milling time. Figure 3 shows the variation of lattice parameter with the refinement of crystallite size of Ni(Si). A lattice parameter expansion of about 1.60% (~5.0% volume expansion) is evident for fcc Ni(Si) when the crystallite size decreased from the bulk state to 11 nm (after 30 h of milling). This corresponds to a 34% reduction in tetragonal shear modulus (from 49 to 32 GPa), calculated based on the equation of state.[19] The increase of lattice parameter with refinement of crystallite size has been reported in a number of pure metals such as Ni, Pd, Cu and Ag,[20–22] which arises due to the well known fact that the interatomic spacing of nanocrystal increases continuously from core to surface due to lattice softening. Therefore, it was not possible to calculate the solubility of Si in Ni as the increase of lattice parameter of later by lattice softening masked the effect of Si dissolution in Ni.

In order to examine the possibility of obtaining Ni(Si) solid solution over a wide composition range, elemental blends of 15, 20, 25 and 28 at. % Si were milled for 30 h. Figure 4 shows the XRD patterns of $x=25$ after different milling intervals. Here, new peaks were observed within 10 h of milling, which were successfully indexed as hexagonal γ-$Ni_{31}Si_{12}$. After 20 h of milling, the powder consisted of a large fraction of $Ni_{31}Si_{12}$, without any residual Si. With continued milling up to 30 h, there was no further change in the XRD pattern except that the relative intensity of the Ni(Si) peak further decreased. The variation of crystallite size of Ni, Si, and $Ni_{31}Si_{12}$ with milling time is shown in Fig. 5. The crystallite size of Ni drops to around 20 nm at the onset of $Ni_{31}Si_{12}$ formation (10 h of milling), whereas the crystallite size of Si still remains above 100 nm. The crystallite size of $Ni_{31}Si_{12}$ has been estimated as 18 nm at the onset of its formation with insignificant change on further milling. Formation of nanocrystalline $Ni_{31}Si_{12}$ (with an average particle size of about 17 nm) has been confirmed from TEM studies of the 30 h milled sample. Figure 6 shows the bright field image and the selected area diffraction pattern corresponding to the $Ni_{31}Si_{12}$ from 30 h milled samples of $x=25$.

The XRD patterns of 15, 20, 25 and 28 at. % Si after 30 h of milling are shown in Fig. 7. It is clear from the XRD patterns in Fig. 7 that small amount of $Ni_{31}Si_{12}$ forms directly during MA even when the nominal composition of the blend is 15 at. % Si and with increase in Si content toward 28 at. % Si, the amount of $Ni_{31}Si_{12}$ increase with a concurrent decrease in the amount of Ni(Si). The fraction of $Ni_{31}Si_{12}$ has been calculated to be about 0.06, 0.14, 0.52, and 0.9 for 15, 20, 25 and 28 at. % Si, respectively. However, the formation of $Ni_{31}Si_{12}$ even at compositions as lean in Si as 15 at. % in the initial blend, must deplete the solute content of the re-

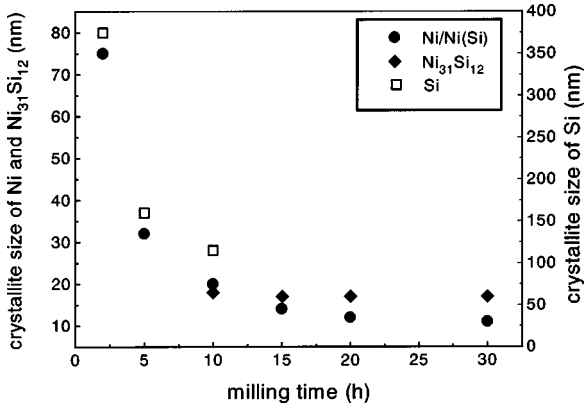

FIG. 5. Variation of crystallite size of Ni, Si, and $Ni_{31}Si_{12}$ with milling time.

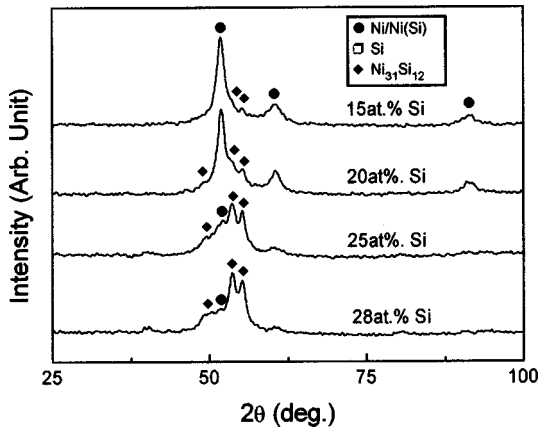

FIG. 7. XRD patterns of 15, 20, 25, and 28 at. % Si after 30 h of milling.

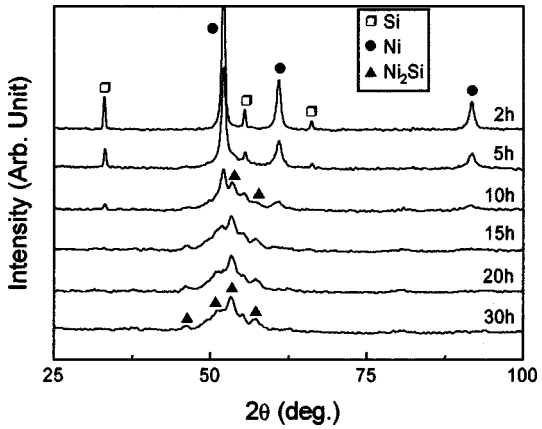

FIG. 8. XRD patterns of 33 at. %Si after different durations of MA.

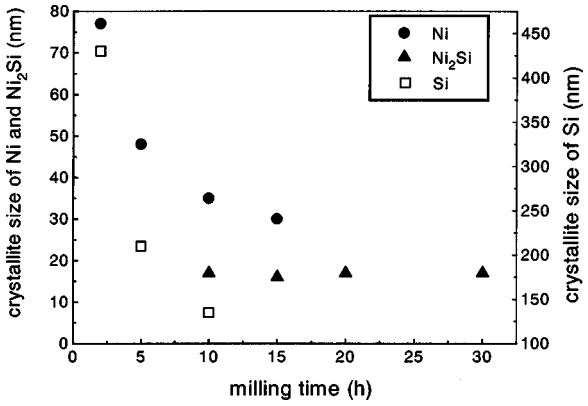

FIG. 10. Variation of crystallite size of Ni, Si and Ni_2Si with milling time for $x=40$.

maining alloy and hence, an extension of solid solubility limit during MA is not evident from the present experiments.

The XRD patterns of $x=25$ and 28 after 30 h of MA (Fig. 7), in the present investigation are similar in nature to those obtained by Jang *et al.*[11] during MA of 24 at. % Si and by Zhou and Bakker,[12] Cho and Koch,[14] and Jang and Tsau[13] after mechanical milling of ordered Ni_3Si. They have suggested the formation of complete fcc solid solution of Si in Ni on milling of Ni_3Si. However, the presence of a major amount of $Ni_{31}Si_{12}$ in the milled samples has been misinterpreted as Ni(Si) in their study. It appears that the disordered Ni_3Si is not stable under high energy ball milling condition and transforms to a metastable phase mixture of Ni(Si) and $Ni_{31}Si_{12}$, which is supported by the results of the present investigation. It is important to note that ordered Ni_3Si could not be obtained during MA in the present study, which is also in conformity with the earlier reports.[8–11]

B. Composition range: $33 \leqslant x \leqslant 50$

In the case of $x=33$, formation of δ-Ni_2Si has been detected after 10 h of milling as shown by the XRD patterns in Fig. 8. Further milling up to 20 h has led to an increase in the fraction of Ni_2Si with a concurrent consumption of Si. The XRD pattern remained unchanged with continued milling up to 30 h. A similar XRD pattern has been reported by Omuro and Miura[10] during MA of Ni and Si mixture with composition 30 at. % Si. Compositions in the range of 37–50 at. % Si have shown similar reaction path, with the formation of Ni_2Si as shown by their 30 h milled samples in Fig. 9. The variation of crystallite size of Ni, Si and Ni_2Si with milling time for $x=40$ is shown in Fig. 10. It has been noticed that the Ni_2Si starts to form (10 h milling) after the crystallite size of Ni drops to 35 nm, when that of Si is still above 100 nm. The crystallite size of Ni_2Si has been estimated as 17 nm at the onset of formation and remains almost constant with further milling. The selected area electron diffraction pattern and bright field image have confirmed the formation of nanocrystalline Ni_2Si (with an average particle size of about 15 nm) as shown in Fig. 11 for $x=40$.

The unidentified XRD peak marked as * in Fig. 9 in the composition range $x=33-50$ suggests the presence of phase(s) other than Ni_2Si in this composition range. In order to identify these peaks better, 30 h milled samples of $x=33-50$ were heat treated at a low temperature (573 K for 4 h) in evacuated glass capsules (10^{-6} Torr). The XRD patterns of heat-treated samples of $x=33$, 37, 40, 45 and 50 are shown in Fig. 12. This treatment has not only sharpened the peaks but also has resulted in additional peaks, which could not be observed in the as milled samples possibly due their

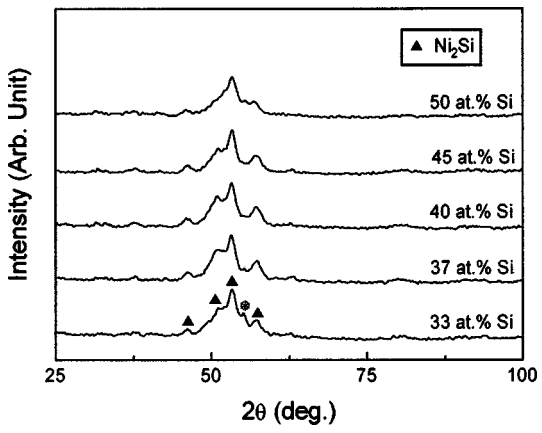

FIG. 9. XRD patterns of 33, 37, 40, 45, and 50 at. % Si after 30 h of milling.

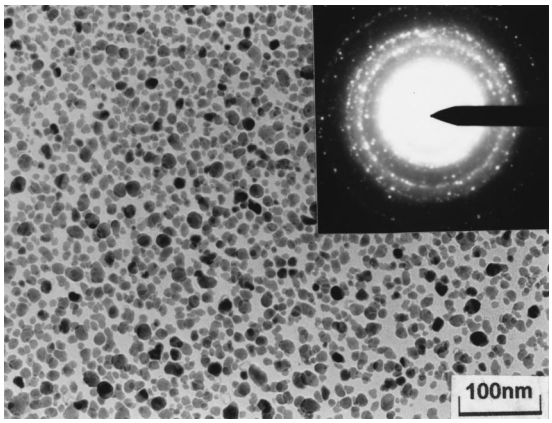

FIG. 11. Transmission electron micrograph and selected area diffraction pattern (inset) of 40 at. %Si after 30 h of MA showing nanocrystalline Ni_2Si.

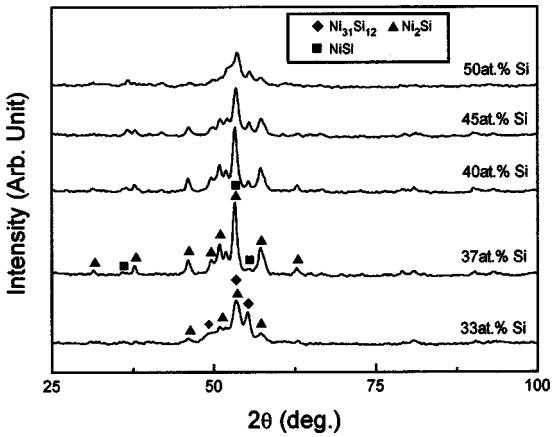

FIG. 12. XRD patterns of the 30 h milled samples of (a) 33, (b) 37, (c) 40, (d) 45, and (e) 50 at. %Si after annealing for 4 h at 573 K.

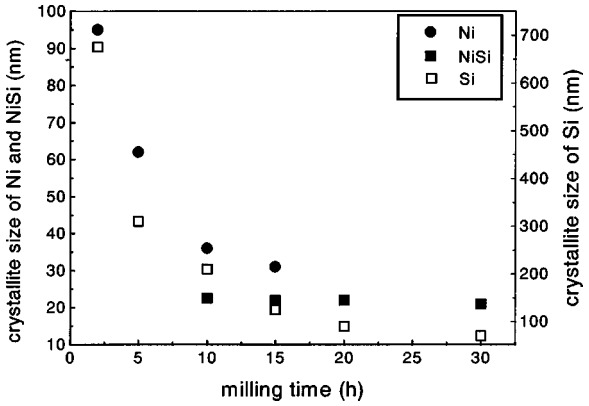

FIG. 14. Variation of crystallite size of Ni, Si, and NiSi with milling time for $x=67$.

low intensity. The XRD peaks of $x=33$ were satisfactorily indexed and correspond to Ni_2Si and $Ni_{31}Si_{12}$ phases and for compositions in the range of $x=37-50$, the peaks could be indexed as Ni_2Si and NiSi phases. The fraction of NiSi has been calculated to be 0.07, 0.12, 0.21 and 0.29 for 37, 40, 45, and 50 at. % Si. Thus, the mechanically alloyed samples show two phase mixtures of $Ni_2Si+Ni_{31}Si_{12}$ in case of $x=33$ and $Ni_2Si+NiSi$ in case of $x=37-50$. It is interesting to note that, although Ni_3Si_2 (40 at. % Si) has a large negative heat of formation (-46 kJ/mol), its formation is bypassed in this composition range during MA.

C. Composition range: $x>50$

MA of Ni–Si blends with a Si content of $x=60$ resulted in η-NiSi formation within 10 h of milling as shown in Fig. 13. After milling for 30 h, the powder consisted of a large fraction of NiSi together with small amount of residual Si. Similar results have been obtained for higher Si content of $x=67$ and 75 during milling (Fig. 13). The fraction of NiSi was found to decrease with increase of Si content as expected from equilibrium phase diagram (0.9, 0.78, and 0.27 for 60, 67 and 75 at. % Si, respectively). Figure 14 shows the variation of crystallite sizes of Ni, Si and NiSi with milling times for $x=67$. The formation of nanocrystalline NiSi ($\sim$22 nm) has been observed when the crystallite size of Ni drops to 35 nm while that of Si is remaining above 100 nm. With further milling, the crystallite size of NiSi remained almost constant. The formation of nanocrystalline NiSi (with an average particle size of about 23 nm) is clear from the TEM bright-field image and selected area diffraction pattern (Fig. 15) obtained from the 30 h milled powder of $x=67$. The formation of $NiSi_2$ could not be observed in the present study even up to 75 at. % Si.

IV. DISCUSSION

It is evident from the present results that during high energy ball milling of a mixture of Ni and Si elemental powders, the elements start to react when the crystallite size of Ni drops in the nanometer regime ($\sim$20–35 nm), while the crystallite size of Si remains much coarser ($>$100 nm). The solid state reaction between Ni and Si during MA results only in congruent melting compounds, namely, $Ni_{31}Si_{12}$, Ni_2Si, and NiSi phases, depending on the Si content in the mixture. It should be noted that, although the heat of formation of the noncongruent melting phase, Ni_3Si_2 (40 at. % Si) is a large negative value, its formation is bypassed even at its stoichiometric composition. Similarly, the present results and those

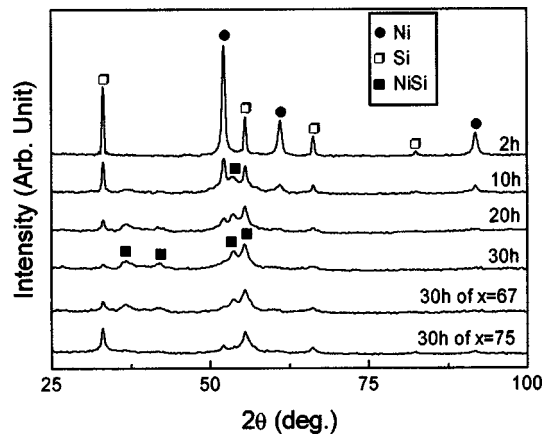

FIG. 13. XRD patterns of $Ni_{40}Si_{60}$ after various milling periods and of 67 and 75 at. %Si after 30 h of milling.

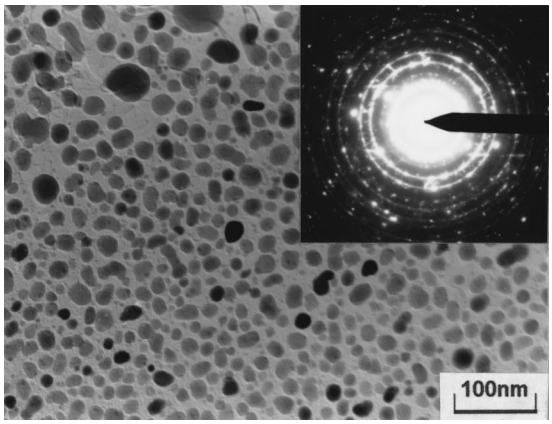

FIG. 15. Transmission electron micrograph and selected area diffraction pattern (inset) of 67 at. %Si milled for 30 h showing nanocrystalline NiSi.

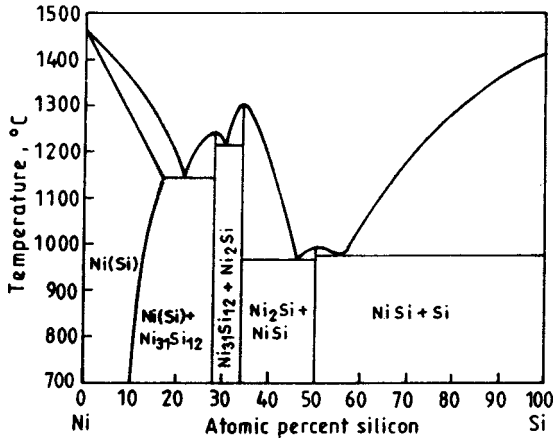

FIG. 16. Metastable Ni–Si phase diagram showing the phase fields in nanocrystalline state after MA.

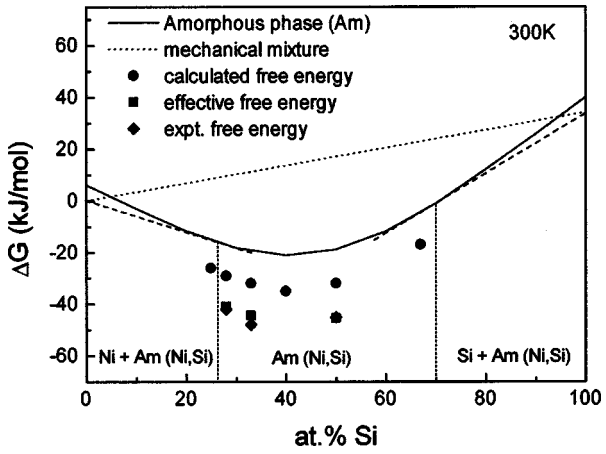

FIG. 17. Gibb's free energy diagram of amorphous phase and intermetallics of Ni–Si binary system.

by the earlier workers[13–15] indicate that the ordered Ni_3Si (noncongruent) is not stable under high-energy ball milling conditions. In contrast, the congruent melting phase ($Ni_{31}Si_{12}$) having a composition closer to the Ni_3Si appears to nucleate and grow. In the absence of formation of Ni_3Si_2, the congruent melting phase mixture (Ni_2Si and NiSi) has been observed to form in the composition range 33–50 at. % Si. Similarly, instead of the $NiSi_2$, the elemental blend has preferred the nucleation and growth of NiSi in Si rich compositions even up to 75 at. % Si. All of the above observations suggested that the formation of congruent melting phases is preferred to noncongruent melting phases over the whole range of composition in nanocrystalline state during MA. Based on the end product compositions of the milled samples (Table II), one can visualize the phase fields in the mechanically alloyed Ni–Si system to be Ni(Si), $Ni(Si)+Ni_{31}Si_{12}$, $Ni_{31}Si_{12}+Ni_2Si$, $Ni_2Si+NiSi$ and $NiSi+Si$ in the composition ranges of 0–10, 10–28, 28–33, 33–50 and 50–100 at. % Si. These phase fields correspond to a metastable phase diagram in the nanocrystalline state of Ni–Si in the absence of noncongruent melting phases, Ni_3Si, Ni_3Si_2, and NiSi as shown in Fig. 16. The volume fraction of different intermetallic phases, calculated from the metastable phase diagram (using lever rule) is shown in Table III with experimental values. In the composition range of 10–28 at. % Si and above 50 at. % Si, it has been noticed that the volume fraction of $Ni_{31}Si_{12}$ below 25 at. % Si and NiSi above 67 at. % Si is much smaller than calculated from the metastable phase diagram, suggesting the nucleation and/or growth of a phase away from its equilibrium phase fields (equilibrium phase fields of $Ni_{31}Si_{12}$ and NiSi is 25–28 at. % Si and 50–67 at. % Si, respectively) is difficult. It is also interesting to note that although NiSi is one of the equilibrium phases in the composition range 40–50 at. % Si, the fraction of NiSi in this above composition range is much smaller than Ni_2Si, suggesting the possible presence of nucleation and/or growth barrier to its formation in the above composition range due to the presence of kinetically more favored Ni_2Si.[23]

TABLE III. Comparison the volume fraction of phases obtained after 30 h of MA and calculated from metastable phase diagram.

Si content after 30 h of milling (at. %)	Phases present after 30 h of MA	Experimentally obtained volume fraction	Volume fraction calculated from metastable phase diagram
13.2	$Ni(Si)+Ni_{31}Si_{12}$	0.06	0.16 ($Ni_{31}Si_{12}$)
18.2	$Ni(Si)+Ni_{31}Si_{12}$	0.14	0.45 ($Ni_{31}Si_{12}$)
22.9	$Ni_{31}Si_{12}+Ni(Si)$	0.52	0.72 ($Ni_{31}Si_{12}$)
25.7	$Ni_{31}Si_{12}+Ni(Si)$	0.90	0.88 ($Ni_{31}Si_{12}$)
35.1	$Ni_2Si+NiSi$	0.07	0.11 (NiSi)
37.0	$Ni_2Si+NiSi$	0.12	0.23 (NiSi)
42.7	$Ni_2Si+NiSi$	0.21	0.58 (NiSi)
48.1	$Ni_2Si+NiSi$	0.29	0.88 (NiSi)
58.3	$NiSi+Si$	0.90	0.83 (NiSi)
65.2	$NiSi+Si$	0.78	0.70 (NiSi)
73.2	$NiSi+Ni$	0.27	0.54 (NiSi)

The solid state reaction between Ni and Si to form a congruent melting phase over a noncongruent melting phase can be understood through thermodynamic consideration. The free energy change for a given phase can be calculated as $\Delta G=\Delta H-T\Delta S$, where ΔH and ΔS are the enthalpy and entropy changes, respectively. To calculate the enthalpy of formation of the intermediate crystalline and the amorphous phases, the thermodynamic model proposed by Miedema and co-workers[17,24] has been used in the present study. The enthalpy change has been expressed by $\Delta H=\Delta H_{ch}+\Delta H_{el}+\Delta H_{st}$, where ΔH_{ch}, ΔH_{el}, and ΔH_{st} are chemical, elastic, and structural contributions and the entropy change was taken as $\Delta S=-R(x_A \ln x_A+x_B \ln x_B)$,[25] where R is the gas constant and x_A and x_B are the atomic concentrations of metals A and B. For the intermetallic compounds, the entropy term has been neglected assuming them to be ordered.

Figure 17 shows the calculated free energy of the intermetallics and amorphous phase at 300 K. The free energy values of the intermetallic phases are represented only by points because all intermediate phases are almost line compounds at their respective stoichiometric compositions. As the free energy of the amorphous phase in a wide range of composition is more negative than that of the mechanical mixture and as Ni is a fast diffuser in Si, (the prerequisite for amorphization is met in the Ni–Si system), an amorphous

phase is expected to form at an early stage of milling.[26,27] The predicted range for the formation of the amorphous phase is shown in Fig. 17. Although no amorphous region has been detected in the present study, it has been proposed by several researchers[28,29] and later identified by several workers[7,30] through TEM investigation that the amorphous phase will be the first phase during solid state reaction between Ni and Si in multilayer diffusion couple experiments, which is very unstable and soon is taken over by crystalline silicides even at room temperature. A careful examination of the metastable phase diagram drawn (Fig. 16) in the present study and the equilibrium phase diagram (Fig. 1) suggests that the congruent melting compounds $Ni_{31}Si_{12}$, Ni_2Si and NiSi are involved in polymorphous or eutectic crystallization reaction, while the noncongruent melting compounds Ni_3Si, Ni_3Si_2 and $NiSi_2$ are not. Therefore, in the present study an amorphous phase close to the nominal composition of the elemental blend probably forms during the early stage of milling, which instantly crystallizes by the mechanically driven crystallization[31,32] into the corresponding congruent melting compounds in the nanocrystalline state (nanocrystallization process).

The fundamental difference between conventional crystallization (coarse grain material) and the nanocrystallization process from amorphous solids lies in the formation of a large volume fraction of interfaces in nanocrystalline materials. The formation of a large volume fraction of interfaces during nanocrystallization has a significant influence on the thermodynamics of phase formation/transformation.[33] The thermodynamic condition for phase α to be stable over metastable phase β is that $G_\alpha < G_\beta$. In the case of nanocrystalline materials, the contribution of interfacial energy term ($\gamma S/V$) to the free energy cannot be neglected as in coarse grained polycrystalline materials. Here, γ is the interfacial energy per unit area, and S and V are the surface and volume, respectively, of a crystallite. In the nanocrystalline state, β may become stable if $G_\alpha + \gamma_\alpha S_\alpha / V_\alpha > G_\beta + \gamma_\beta S_\beta / V_\beta$.[34] In other words, if the rate of increase of free energy with decrease in crystallite size of α phase is higher than that of the β phase, the latter will become stable over the former below a critical crystallite size. The above condition implies that with decreasing crystallite size, the phase with the lower interfacial energy term becomes energetically favored. From much experimental evidence based on HREM studies,[33] it has been established that the polymorphous and eutectic nanocrystallization products, controlled by the energetic process, exhibit specific orientation relationships between neighboring nanograins. These interfaces are of low energetic configurations characterized by coherent or semicoherent boundaries, containing very small excess volume. On the other hand, the peritectic or peritectoid reaction products, controlled by an atomic diffusion process, always contain randomly oriented nanocrystallites of relatively higher energetic configuration characterized by incoherent interfaces. The interfacial energy of coherent and incoherent solid–solid interfaces are about 0.5 and $0.9E_B$ (E_B is high angle grain boundary energy), respectively.[7] Thus, the nanocrystalline state appears to favor the congruent melting compounds of low energy interfaces over the noncongruent melting phases of higher energy interfaces below certain crystallite size. It has been identified[35] that the noncongruent melting compound will be stable in bulk state (above 100 nm) where interfacial energy contribution to the free energy is negligible.

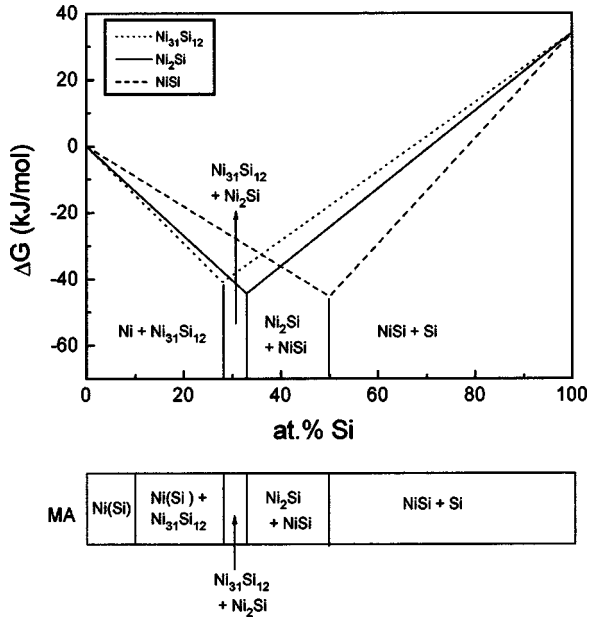

FIG. 18. Effective free energy diagram for congruent melting phases in the Ni–Si system showing the predicted phase fields in comparison to those obtained by MA (bar diagram).

To understand the phase fields obtained by MA, the effective free energy model proposed by Desra and Yavari[36] has been used in the present study. Since the formation of noncongruent melting compounds is bypassed during milling, only the free energy associated with congruent melting phases needs to be considered. If $\Delta G_{\rm pc}$ is the free energy associated for polymorphous crystallization to congruent melting phase, the effective free energy of congruent melting phases can be expressed as $\Delta G_e = \Delta G_c + \Delta G_{\rm pc}$, where ΔG_e and ΔG_c are the effective and calculated (from Miedema's model) free energy of intermetallic, respectively. The free energy values of the intermetallics in Fig. 17 are the effective free energy ΔG_e values, which are very close to the experimental ones.[17] However, for a more realistic case, the driving force for crystallization of composition C to congruent melting phases of composition C*, i.e., free energy associated with a concentration fluctuation $\Delta G_{\rm fl}$, should be considered, which modifies the effective free energy as $\Delta G_e = \Delta G_c + \Delta G_{\rm pc} + \Delta G_{\rm fl}$.[36] The free energy associated with concentration fluctuation can be expressed as[36]

$$\Delta G_{\rm fl}(\mathrm{C}) = 0.5(\mathrm{C}-\mathrm{C}^*)^2 \partial^2 \Delta G / \partial C^2,$$

where $\partial^2 \Delta G / \partial C^2$ is the second derivative of free energy with composition.

The effective free energy of congruent melting phases at room temperature, calculated based on the above formalism, is shown in Fig. 18 along with the predicted phase fields, which are quite comparable to those obtained in nanocrystalline state during MA (bar diagram in Fig. 18).

However, it should be noted that in the present calculation the interfacial free energy term ($\gamma S/V$) associated with

the refinement of crystallite size is not considered. As the crystallite size (represented by the surface to volume ratio, S/V) and interfacial energy (γ) characterized by coherent or semicoherent boundary, of different congruent melting phases after 30 h MA are comparable, the interfacial energy term ($\gamma S/V$) will be almost similar in each case. Thus, the increase in free energy of congruent melting phases due to interfacial energy term ($\gamma S/V$) is expected to be of the same order for all the silicides. Therefore, it is expected that the phase fields obtained from thermodynamic calculations without including the interfacial free energy of congruent melting phases are very close to those with the inclusion of the latter.

V. CONCLUSIONS

MA has lead to the formation of only congruent melting silicides ($Ni_{31}Si_{12}$, Ni_2Si and NiSi) in the nanocrystalline state and the noncongruent melting compounds (Ni_3Si, Ni_3Si_2 and $NiSi_2$) where bypassed in this system even at their equilibrium phase fields.

During MA, Ni silicides start to form when the crystallite size of Ni drops to the nanometer regime ($\sim$20–30 nm), while the Si remains in bulk state.

A lattice parameter expansion of 1.6% (volume expansion of 5%) is evident for fcc Ni(Si) when the crystallite size decreased from bulk state to nanometer scale.

The phase formation during MA is quite analogous to polymorphous or eutectic nanocrystallization reaction from an amorphous phase. The nanocrystallization reaction favors the formation of congruent melting compounds over noncongruent melting compounds due to lower interfacial energy which plays an important role in the stability of phases in nanocrystalline materials.

The predicted phase fields obtained from effective free energy calculations are quite close to those obtained in the nanocrystalline state during MA.

ACKNOWLEDGMENTS

The financial support from the Department of Science and Technology and Aeronautical Research and Development Board, The Government of India is gratefully acknowledged.

[1] B. S. Murty and S. Ranganathan, Int. Mater. Rev. **43**, 101 (1998).
[2] C. C. Koch, Nanostruct. Mater. **9**, 13 (1997).
[3] F. H. Froes, C. Suryanarayana, K. Russell, and C. G. Li, Mater. Sci. Eng., A **192/193**, 612 (1995).
[4] H. J. Fecht, Nanostruct. Mater. **6**, 33 (1995).
[5] R. Pretorius, T. K. Maris, and C. C. Theron, Mater. Sci. Eng., R. **10**, 1 (1993).
[6] L. A. Clevenger and C. V. Thompson, J. Appl. Phys. **68**, 1325 (1990).
[7] W. H. Wang and W. K. Wang, J. Mater. Res. **9**, 401 (1994).
[8] K. Omuro and H. Miura, Jpn. J. Appl. Phys., Part 2 **30**, L851 (1991).
[9] A. P. Radlinski and A. Calka, Mater. Sci. Eng., A **134**, 1376 (1991).
[10] K. Omuro and H. Miura, Appl. Phys. Lett. **60**, 1433 (1992).
[11] J. S. C. Jang, C. H. Tsau, W. D. Chen, and P. Y. Lee, J. Mater. Sci. **33**, 265 (1998).
[12] G. F. Zhou and H. Bakker, Acta Metall. Mater. **42**, 3009 (1994).
[13] J. S. C. Jang and C. H. Tsau, J. Mater. Sci. **28**, 982 (1993).
[14] Y. S. Cho and C. C. Koch, J. Alloys Compd. **194**, 287 (1993).
[15] T. B. Massalski, *Binary Alloy Phase Diagram*, 2nd ed. (ASM, Metals Park, OH, 1990), Vol. 3, p. 2859.
[16] Th. H. de Keijser, J. I. Langford, E. I. Mittemeijer, and A. B. P. Vogels, J. Appl. Crystallogr. **15**, 308 (1982).
[17] F. R. de Boer, R. Boom, W. C. M. Mattens, A. R. Miedema, and A. K. Nissen, *Cohesion in Metals*, edited by F. R. de Boer and D. G. Pettifor (Elsevier, North Holland, Amsterdam, 1988), Vol. 1.
[18] W. B. Pearson, *A Handbook of Lattice Spacing and Structures of Metals and Alloys* (Pergamon, London, 1958), p. 786.
[19] J. L. Tallon, Nature (London) **342**, 658 (1989).
[20] X. D. Liu, K. Lu, H. Y. Zhang, and Z. Q. Hu, J. Phys.: Condens. Matter **6**, L497 (1994).
[21] M. R. Fitzimmons, J. A. Eastman, M. M. Stach, and G. Wallner, Phys. Rev. B **44**, 2452 (1991).
[22] S. Onodera, J. Phys. Soc. Jpn. **61**, 2190 (1992).
[23] U. Gosele and K. N. Tu, J. Appl. Phys. **53**, 3252 (1982).
[24] W. Weeber and H. Bakker, Physica B **153**, 93 (1988).
[25] J. M. Lopez, J. A. Alonso, and L. J. Gallego, Phys. Rev. B **36**, 3716 (1987).
[26] P. H. Shingu and K. N. Ishihara, J. Alloys Compd. **194**, 319 (1993).
[27] R. B. Schwartz and W. L. Johnson, Phys. Rev. Lett. **51**, 415 (1983).
[28] R. W. Walser and R. W. Bene, Appl. Phys. Lett. **28**, 624 (1976).
[29] A. Hiraki, Jpn. J. Appl. Phys., Part 1 **22**, 549 (1983).
[30] E. Ma, W. J. Meng, W. L. Johnson, M. A. Nicolet, and M. Nathan, Appl. Phys. Lett. **53**, 2033 (1988).
[31] N. Q. Wu, J. M. Wu, Z. Z. Li, and G. X. Wang, Mater. Trans., JIM **38**, 255 (1997).
[32] M. L. Traudeau, R. Schulz, D. Dussault, and A. Van Neste, Phys. Rev. Lett. **64**, 99 (1990).
[33] K. Lu, Mater. Sci. Eng., R. **16**, 161 (1996).
[34] V. G. Grayznov and L. I. Trusov, Prog. Mater. Sci. **37**, 289 (1993).
[35] M. K. Datta, S. K. Pabi, and B. S. Murty, Mater. Sci. Eng. A. (in press).
[36] P. J. Desra and A. R. Yavari, Phys. Rev. Lett. **64**, 1533 (1990).